



Revisiting the carbon mesopore contribution towards improved performance of ionic liquid–based EDLCs at sub-zero temperatures

V. Pavlenko^{1,2,3,4} · S. Kalybekkyzy² · D. Knez⁵ · Q. Abbas⁶ · Z. Mansurov^{3,4} · Zh. Bakenov^{1,2} · A. Ng¹

Received: 13 August 2021 / Accepted: 25 October 2021 / Published online: 6 November 2021
© The Author(s) 2021

Abstract

The important role of mesopores has been investigated in electric double-layer capacitors (EDLCs) operating from 24 °C down to –40 °C by using two in-house synthesized carbons with hierarchical porosity. These carbons were prepared from colloidal nanoparticles of SiO₂ as the template and D-glucose as the carbon source. A decrease in the average diameter of the nanoparticles from 12 to 8 nm results in increased surface area and offers a perfect match between ions of binary mixture of imidazolium-based fluorinated ionic liquids and the pores of carbon. Short-range graphene layers produced with 8-nm silica nanoparticles lead to the creation of transport channels which better accommodate ions. We explain these findings per coulombic interactions among the ions and between the pore wall and the ionic species under confinement and electrochemical polarization conditions. Further, it is shown that a microporous carbon (another in-house produced rice-husk carbon $S_{\text{BET}} = 1800 \text{ m}^2 \cdot \text{g}^{-1}$) performs better than hierarchical carbons at room temperature; however, thanks to the large fraction of mesopores, the latter exhibit far higher capacitance down to –40 °C. While the ordering of ions in confinement is more critical at room temperature and dictated by the micropores, low temperature performance of supercapacitors is determined by the mesopores that provide channels for facile ion movement and keep the bulk ionic liquid–like properties.

Keywords Electric double-layer capacitor · SiO₂-templated carbon · Ionic liquid · Coulombic ordering · Mesopore · Low temperature

Introduction

Application of ionic liquids (ILs) in electrochemical capacitors is very promising due to the possibility of a significant increase in stability window and consequently improved energy density [1, 2]. In addition, by using ionic liquids, one would get rid of the problem of toxic and flammable solvents, e.g., acetonitrile. Despite their several advantages, ionic liquids possess a high viscosity which hinders their low temperature applications [3, 4]. The issue of ionic liquids freezing at relatively higher temperatures has been solved by using their eutectic mixtures [3, 5] which do not undergo crystallization and only display glass transition down to low temperatures ca. –40 °C [6]. In such IL mixtures, decreased crystal lattice energy as well as the melting point is due to the inefficient ion packing caused by the bulky cation with low degree of symmetry [6, 7]. Another factor that influences electric double-layer capacitor (EDLC) performance is the ion sieving effect imposed by the large fraction of ultramicropores ($d < 0.7 \text{ nm}$) in majority of nanoporous carbons, which are smaller than the dimensions of IL cations

✉ Q. Abbas
qamar.abbas@tugraz.at

✉ A. Ng
annie.ng@nu.edu.kz

¹ Department of Electrical and Computer Engineering, Nazarbayev University, Nur-Sultan 010000, Kazakhstan

² National Laboratory Astana, Nazarbayev University, Nur-Sultan, Kazakhstan

³ Al-Farabi Kazakh National University, 71, al-Farabi ave, Almaty 050040, Kazakhstan

⁴ Institute of Combustion Problems, 172, Bogenbay Batyr str, Almaty 050009, Kazakhstan

⁵ Graz Centre for Electron Microscopy, Steyrergasse 17, 8010 Graz, Austria

⁶ Institute for Chemistry and Technology of Materials, Graz University of Technology, Stremayrgasse 9, 8010 Graz, Austria

(e.g., EMIM ~ 1.0 nm) [8, 9]. From this point of view, an abundance of mesopores seems to be advantageous for IL-based charge storage applications. Nevertheless, increase in the pore diameter usually results in low density materials and thereby low volumetric capacitance.

Given a wide range of carbon mesopores (from 2 to 50 nm according to the IUPAC), their presence favors high amount of charge storage in electrolytes such as ILs where relatively large size of ionic species is adapted for big pores. It has been shown by using TiC-CDCs with average pore size of 0.7 nm and 1.0 nm in ILs that even a slight volumetric difference can strongly influence the inter-ion and pore wall-ion interactions [10]. Difference in the pore size can affect the capacitance performance as well as the rate capability of the carbon-based energy storage devices [11]. While the neat ILs form long-range layered structures along the pore wall under the charge overscreening, the ionic order in these ILs can be disturbed either with a solvent [12] or by using IL binary mixtures taking benefit from the absence of crystallization due to the difference in ion size; e.g., the cations do not fit into the anionic lattice and/or the anions do not completely participate in the crystal structure [7]. Overall, the factors such as presence of small ordered pores facilitate in creating a so-called superionic state (where image charge drives easier packing of ions with the same sign) [13, 14]. Also, the absence of overscreening leads to a strong ion-pore wall interaction under confinement [15], or the breakdown of electroneutrality in nanopores [16]. The second factor that may break ionic organization is mixing of ILs to disturb the alternative arrangement of ions [17, 18] which may be even more pronounced for the electrified nanopores with confined ionic species.

Suspensions of silica nanoparticles have been used as hard template with various organic precursors to prepare carbons with hierarchical porosity. In general, the first step of preliminary carbonization (silica template and organic precursor mixture) at ~ 500 °C in inert atmosphere is followed by a typical leaching of formed inorganic templates by diluted acids (e.g., HCl, H₂SO₄). An EDLC using SiO₂-templated carbon having a surface area (S_{BET}) of only 1065 m²·g⁻¹ and IL mixture as electrolyte demonstrated a gravimetric capacitance of 144 F·g⁻¹ at room temperature [19]. By contrast, other works have demonstrated relatively lower capacitance of 120 F·g⁻¹ (~ 30 F·g⁻¹ per total mass of electrodes) has been achieved with EDLCs using IL and activated carbons of $S_{\text{BET}} = 2000 \text{ m}^2 \cdot \text{g}^{-1}$ [20–22]. In the context of pore size and surface area of carbons versus the capacitance, these performance differences may arise due to the confinement effect in nanopores which is more influenced by the pore structure and electrochemical polarization conditions [23].

Here, SiO₂-based porous carbons obtained via an optimized template synthesis have been investigated in symmetric supercapacitors with the mixture of ILs ([EMIm]

[FSI]_{0.5} [BF₄]_{0.5}) as an electrolyte. The performance of supercapacitors is evaluated at room temperature and down to – 40 °C. This work takes the benefit from lower melting temperature of binary ionic liquid in ionic liquid mixtures due to the difference in alkyl chain structures [24, 25]. These findings validate the influence of carbon nanoporous structures on the ordering of ions which is disturbed due to the different confinement effects on layered ionic arrangement along the pore walls. Further, in carbons where mesopores are adapted for ionic movement and electrolyte maintains bulk-like properties, EDLCs display excellent capacitance retention down to – 40 °C. This work presents a realistic set of performance data for hierarchical carbons and ionic liquid-based EDLCs and compare with an in-house produced microporous carbon.

Experimental

Preparation of porous carbon materials

The two types of porous carbons labelled as “SGT_{12nm}” and “SGT_{8nm}” were produced using 40 wt.% suspension of 12 nm colloidal silica (Ludox HS-40 supplied from Sigma-Aldrich) and 30 wt.% suspension of 8 nm colloidal silica (Ludox SM-30 supplied from Sigma-Aldrich) respectively in water as hard templates. D-Glucose (reagent grade, supplied from Laborpharma LTD) was used as the carbon source in both cases. It was mixed in a jar with the colloidal suspension of silica at a mass ratio of 1:1. Herein, 9 g of D-glucose was mixed either with 22.5 g of 40 wt.% suspension of 12 nm colloidal silica, or with 30 g of 30 wt.% suspension of 8 nm colloidal silica. After mixing, the samples were dried at 160 °C for 8 h to prevent caramelization. The dried mixtures of colloidal silica with glucose were pyrolyzed up to 800 °C at a rate of 10 °C·min⁻¹ for a dwell time of 2 h in a muffle furnace (VBF-1200X-H8) under 100 cm³·min⁻¹ nitrogen (N₂, 99.99 wt.%) flow. The carbonized mixtures were cool down until reaching the room temperature before further treatment. The resulting carbon-silica composites were stirred in 100-mL solution of NaOH (reagent grade, supplied from Laborpharma LTD) with a concentration of 3 mol·L⁻¹ under reflux at 100 °C for 24 h. The obtained carbon material was then filtered from alkaline solution and washed few times with hot distilled water (conductivity = 0.5 μS/cm) until the pH became neutral. This procedure of leaching and washing was repeated two times to ensure complete separation of carbon materials from the silica templates. The samples were finally dried at 120 °C for 24 h under reduced pressure.

The microporous carbon samples labelled as RHC were produced by carbonization and subsequent chemical activation of rice-husk (RH, purchased from Kyzylorda Region,

Kazakhstan). Typically, RH was subjected for cleaning using the tap water and drying at 90 °C for 48 h to a constant mass before its preliminary carbonization at 500 °C ± 10 °C under nitrogen atmosphere for 40 min. The chemical activation was performed by mixing of the carbonized materials with dry KOH (reagent grade, supplied from Laborpharma LTD) in a weight proportion of the alkali to carbonise equal to 2:1, followed by the pyrolysis of resulting mixture in a stainless-steel crucible at 800 °C ± 10 °C with a dwell time of 1 h under nitrogen flow (100 cm³·min⁻¹). The obtained mixture after activation and cooling was then subjected to decantation by using cold tap water with subsequent washing using hot deionized water in order to reach a neutral pH. The final obtained carbons were then dried under reduced pressure at 110 °C for 24 h.

Physicochemical characterization

Before the nitrogen gas adsorption analysis, each carbon sample (ca. 80 mg) was degassed under vacuum at 350 °C for 12 h. The adsorption/desorption isotherms were obtained by Autosorb-1 (Quantachrome Instruments, UK) in a range of relative pressures from 0.005 to 0.991 at -196 °C. The surface area was calculated from the range of relative pressure values below 0.1 by using the Brunauer–Emmett–Teller (BET) method, cumulative DFT method, as well as BJH method.

The images of transmission electron microscopy (TEM) and selected area electron diffraction (SAED) were obtained by using a FEI Tecnai F20 microscope, operating at a voltage of 200 kV. The TEM is equipped with a high-resolution Gatan imaging filter including a 2048 pixels × 2048 pixels UltraScan CCD camera for capturing the micrographs. Zero-loss filtering with a slit-width of 15 eV was applied during image and SAED acquisition to enhance contrast and image quality. The TEM samples were prepared by dispersing carbon materials in ethanol (ethyl alcohol > 99.9 wt.%, supplied from Laborpharma LTD) followed by a 1-min ultrasonication step. One droplet of the dispersion was cast on Quantifoil R3/3 copper TEM grids and subsequently dried on a hotplate at 100 °C. Raman spectra were measured on a Horiba Jobin Yvon LabRam 800 HR spectrometer equipped with a 1024 × 256 CCD (Peltier-cooled) and an Olympus BX41 microscope. A laser wavelength of 633 nm was used for all measurements.

EDLC construction and electrochemical testing

The electrodes in the form of pellets with an average mass of 12 mg were prepared from a mixture of 85 wt.% carbon, 10 wt.% polytetrafluoroethylene (60 wt.% suspension in water, supplied from Sigma-Aldrich), and 5 wt.% conductivity enhancer (C-65 supplied from TIMCAL). The

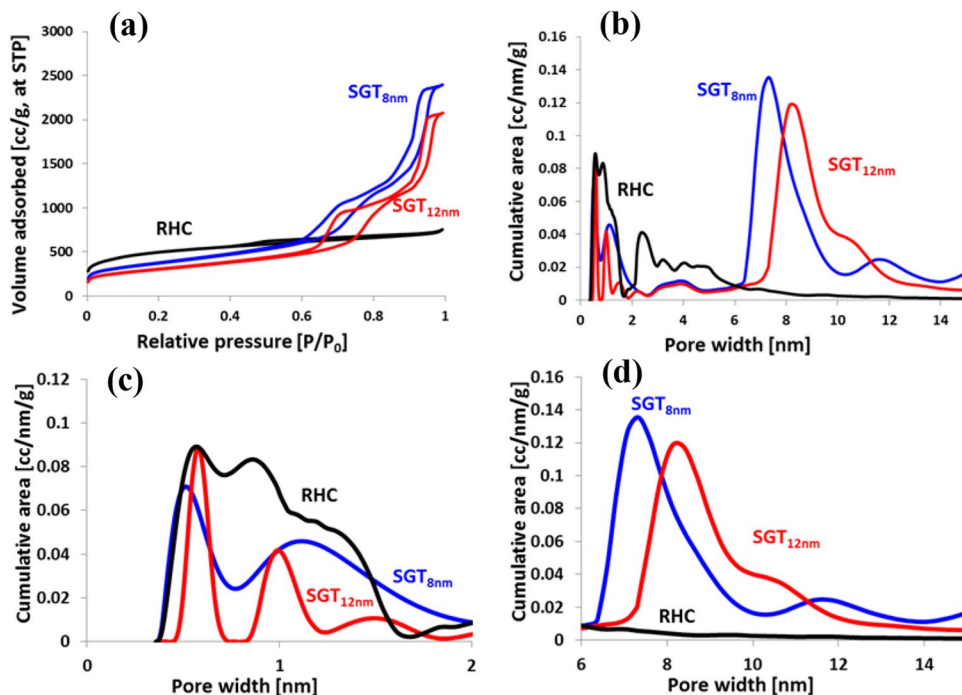
mixture was placed in a beaker where a small amount of isopropanol (99.5 wt.% supplied from Laborpharma LTD) was added under stirring until the most part of isopropanol is evaporated. Hereinafter, the resulting homogenized mixture was rolled into sheets with ca. 200-µm thickness on a glass plate. Then, these electrodes were vacuum dried overnight at 120 °C and placed in a glovebox (MBRAUN, H₂O and O₂ < 1 ppm). All the carbons were tested in EDLCs with symmetric configuration. Supercapacitor cells were fabricated in two-electrode coin cell (cell type CR2032), with Whatman ® glass microfiber filter (grade GF/A supplied from Sigma-Aldrich) used as a separator. The electrolyte EMIm [BF₄]_{0.5} [FSI]_{0.5} was prepared by mixing 1:1 molar ratio of ILs (1-ethyl-3-methylimidazolium tetrafluoroborate, [EMIm][BF₄] (99.0%, H₂O < 20 ppm, from Sigma-Aldrich) and 1-ethyl-3-methylimidazolium bis(fluorosulfonyl)imide ([EMIm][FSI] (99.9% purity, H₂O < 20 ppm, from Solvionic). The electrochemical measurements were carried out with a multichannel potentiostat/galvanostat VMP-3 from Biologic Science Instruments. The gravimetric capacitance was calculated from the discharge curve of the EDLCs by using the formula: $C = (2)I/[(dU/dt)m_{am}]$, where I is the current (A), dU/dt is the discharge curve slope (V·s⁻¹), and m_{am} is the mass of active carbon in one electrode (in gram). The electrochemical tests at selected temperatures of -40 °C, -20 °C, 0 °C, and 24 °C were carried out in a benchtop temperature humidity test chamber (XiAn LIB Environmental Simulation Industry). During constant power tests, the supercapacitor cells were discharged at a selected power in the voltage range from 3.0 to 1.5 V (see Figure S2b). The specific power and energy values are presented in Ragone plot.

Results and discussion

Herein, physicochemical and electrochemical investigations have been performed on three carbon materials, namely SGT_{12nm} and SGT_{8nm} and RHC. Adsorption/desorption isotherms indicating the nitrogen uptake by pristine carbons at -196 °C are shown in Fig. 1a. The isotherm of RHC can be referred to type I indicating a precipitous rise of nitrogen adsorption in the range of low relative pressure which is a typical characteristic of microporous materials, but with relatively broad pore size distributions including wider micropores and possibly narrow mesopores [26, 27]. Nevertheless, an existence of slightly expressed hysteresis loop suggests that this isotherm can be also attributed to type IV as it shows an increase in the volume of nitrogen adsorbed at higher relative pressure.

In contrast, the isotherms of SGT_{12nm} and SGT_{8nm} exhibit a combination of types I and IV, while the latter indicates an increase in the volume of nitrogen adsorbed at

Fig. 1 **a** N_2 adsorption/desorption isotherms measured at $-196\text{ }^\circ\text{C}$. **b** QLDFT pore sizes of the carbon materials SGT_{12nm}, SGT_{8nm}, and RHC. **c** The microporous region (up to 2.0 nm) enlarged from “b”. **d** The magnified mesoporous region from 6 to 15 nm from “b”



higher relative pressure. According to the IUPAC classification, desorption branches of the isotherms corresponding to SGT_{12nm} and SGT_{8nm} can be attributed to the H2(b) and H1 hysteresis loops, respectively, which correspond to the multilayer nitrogen adsorption in the mesopores. In turn, type H1 represents porous materials with a narrow distribution of regular, well-defined cylindrical-like pores [26], while the H2(b) can be attributed to the pore blocking effect which can arise due to the “ink-bottle” shape of pores, although their size is relatively wide. Table 1 shows the surface and porous characteristic of SGT_{12nm} and SGT_{8nm} carbons which exhibit high values of total pore volume of $2.85\text{ cm}^3\cdot\text{g}^{-1}$ and $3.5\text{ cm}^3\cdot\text{g}^{-1}$, respectively, with a prevailing part belonging to mesopores (up to 85%). The average pore width is centered at 8.4 nm for SGT_{12nm} and at 7.2 nm for SGT_{8nm}, respectively. It is noteworthy that both templated carbon materials possess a well-defined width of mesopores arising due to relatively uniform sizes of the silica nanoparticles used as hard templates. Consequently, these carbon materials exhibit the highest volumes of mesopores and limited volumes of

micropores, allowing to distinguish their positive impact on the performance of EDLCs at low temperatures.

SGT_{8nm} displays higher surface area compared to SGT_{12nm} which is related with the smaller size of silica nanoparticles used during the synthesis step. By contrast, the microporous RHC carbon has a high BET and cumulative surface area ($S_{\text{BET}} = 1801\text{ m}^2\cdot\text{g}^{-1}$ and $S_{\text{DFT}} = 1670\text{ m}^2\cdot\text{g}^{-1}$ respectively), with a total pore volume of $1.04\text{ cm}^3\cdot\text{g}^{-1}$. The pore size distribution of RHC (Fig. 1b, c) shows a high fraction of micropores with a diameter between 0.7 and 1.5 nm. The pore structure of RHC consists mainly of narrow pores connected to bigger micropores just below 2.0 nm. Overall, the micropore volume of RHC consists of around 67% of the total porosity and the remaining fraction is dominated by the big micropores and to some extent the mesopores which can act as transport channels for ionic species.

In contrast to RHC, and as described earlier, SGT_{8nm} and SGT_{12nm} possess large fraction of mesopores. However, Fig. 1c and d show the presence of micropores in SGT_{8nm} which are connected to a relatively large fraction of mesopores via intermediate size pores forming channels.

Table 1 Porosity data of the hierarchical carbon materials SGT_{12nm}, SGT_{8nm}, and activated carbon originating from rice husk (RHC)

Sample	$S_{\text{BET}}\text{ (m}^2\cdot\text{g}^{-1}\text{)}$	$S_{\text{DFT}}\text{ (m}^2\cdot\text{g}^{-1}\text{)}$	$S_{\text{BJH}}\text{ (m}^2\cdot\text{g}^{-1}\text{)}$	Micropore volume ($\text{cm}^3\cdot\text{g}^{-1}$)	Total pore volume ($\text{cm}^3\cdot\text{g}^{-1}$)	Fraction of mesopores (%)
SGT _{12nm}	1069	1123	1086	0.42	2.85	85.3
SGT _{8nm}	1319	1339	1319	0.52	3.50	85.2
RHC	1801	1670	1790	0.72	1.04	32.8

On the other hand, slight differences in pore size distribution between SGT_{8nm} and SGT_{12nm} exist with latter showing two peaks in the microporous region that could mean development of different types of transport channels. In the case of SGT_{12nm}, the porosity is dominated by considerable amount of ultramicropores (below 0.7 nm) while some fraction of pores exist around 1.0 nm. While SGT_{8nm} possesses relatively high fraction of pores between 0.7 and 2.0 nm (also indicated by its high surface area, $S_{\text{BET}} = 1319 \text{ m}^2 \cdot \text{g}^{-1}$), SGT_{12nm} shows small fraction of micropores $\sim 1.0 \text{ nm}$ and a lower surface area ($S_{\text{BET}} = 1069 \text{ m}^2 \cdot \text{g}^{-1}$).

Figure 2 shows TEM results where both templated samples can be identified as possessing layers of graphene from the TEM bright-field micrographs. However, slight qualitative differences between SGT_{12nm} and SGT_{8nm} can be discerned regarding the size of these layers, which is consistent with the gas adsorption data. From the intensity profiles, obtained via the regions highlighted in the corresponding TEM images, the typical interlayer distance value for graphite (as given in the intensity profile graphs) is measured. Morphology of the resulting carbons is represented by the graphene-like layers that are locally arranged in parallel, forming a typical pattern of activated and porous carbons. In turn, the areas allocated in the space between the layers can be attributed to the intraparticle mesopores resulted from the leaching of silica nanoparticles and leaving behind carbon shells. The short-range graphene layers of SGT_{8nm} favor the formation of smaller pores and transport channels

as well as the enhanced surface area as discussed in the “gas adsorption” section. In case of SGT_{12nm}, relatively large graphene layers are developed that are oriented to form bigger pores or mesopores while only small fraction contributes to the micropores. Hence, big spaces lead to larger pores and consequently low surface area for SGT_{12nm} as indicated in gas adsorption data. Note that the small pores in SGT_{8nm} are appearing throughout the structure, however, in case of SGT_{12nm}, the small pores are only formed via random arrangement of graphene layers. Overall, TEM data qualitatively supports the previously discussed isotherms and the pore size distribution data of hierarchical carbons.

A slight deviation of the measured value (0.35 nm) to values reported in literature for nanocrystalline graphite (0.34 nm) is within the margin of error, considering a pixel size of the images of approximately 0.02 nm [28]. The inset shows selected area electron diffraction (SAED) data obtained from a larger agglomeration of the graphene layers and exhibit their typical ring features. The blurry appearance can be explained with the small size of the contributing, randomly oriented layers. Overall, the surfaces of both the carbons are uneven and strongly developed, where the mesopores are clearly visible.

Raman spectra in Figure S4 and derived structural parameters of three carbons in Table 2 show a clear difference between the RHC and hierarchical carbons. While the RHC possesses distinct D- and G-band typical for activated carbons and positioned at 1600 cm^{-1} and 1348 cm^{-1} , the

Fig. 2 TEM bright-field image of “graphitic carbon agglomerates” for (a) SGT_{12nm} and (b) SGT_{8nm}; green and blue rectangle highlights the region from which intensity profiles were extracted to measure the interlayer distance of graphene indicated. Inset of (a) illustrates a selected area electron diffraction (SAED) where graphene layers display a similar pattern which is typical for nanocrystalline graphite. A rotational averaged intensity graph is superimposed in red showing the features as peaks

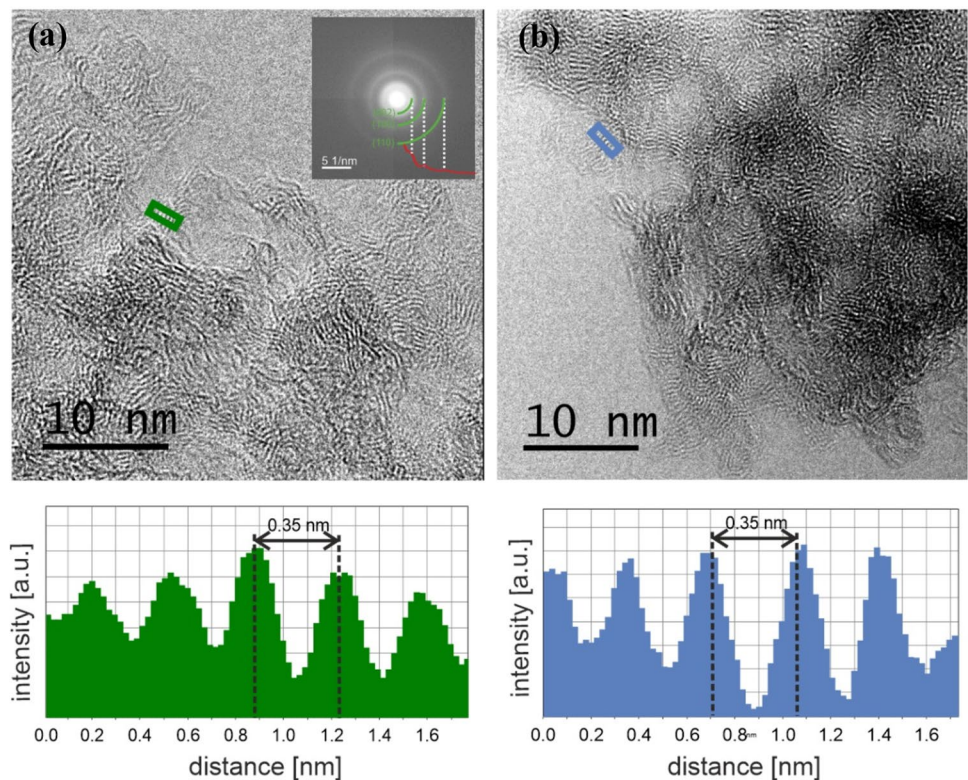


Table 2 D- and G-band parameters of three carbon materials; ω_G , G-band position; ω_D , D-band position; Γ_G , G-band width; Γ_D , D-band width, and I_D/I_G , D-/G-band intensity ratio

	ω_G	ω_D	Γ_G	Γ_D	I_D/I_G
SGT _{12nm}	1605	1340	33	70	0.97
SGT _{8nm}	1604	1339	32	72	0.95
RHC	1600	1348	44	67	0.97

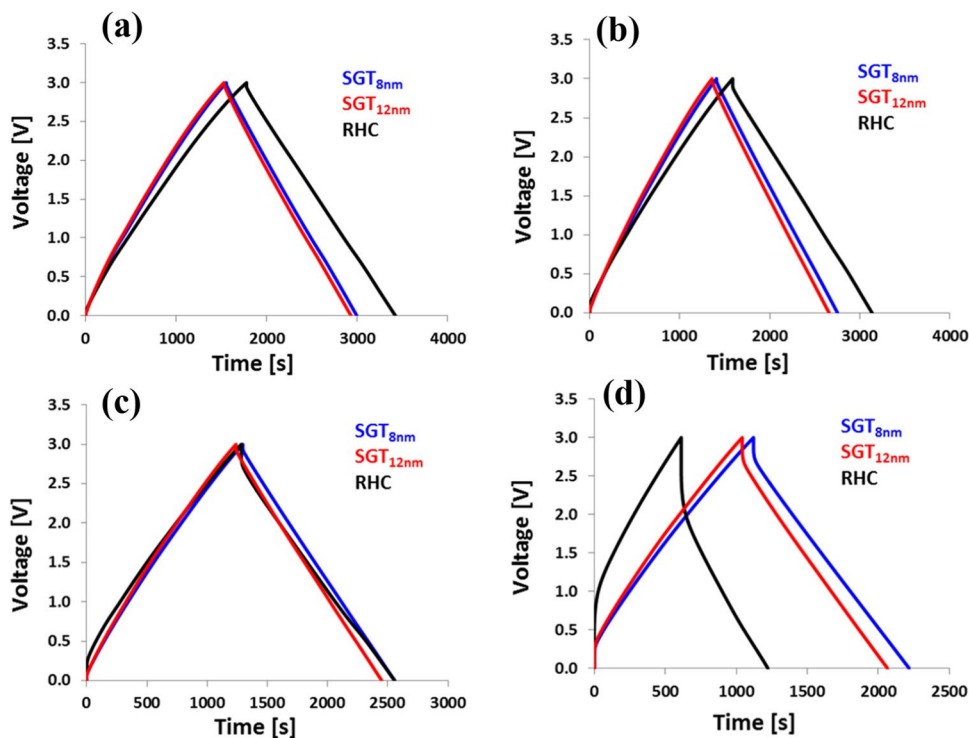
positions and the band width are shifted in SGT_{12nm} and SGT_{8nm}. A comparatively high G-band position indicates change in the E_{2g} vibration mode of graphitic layers in hierarchical carbons and a more graphene-like structure [29–32]. The narrow G-band in these carbons indicates improved in-plane coherence associated with ordered structure. This is further confirmed by the shoulder peaks at $\sim 1653\text{ cm}^{-1}$ for SGT_{12nm} and SGT_{8nm} characteristic of layered graphene framework. On the other hand, G-band width and D-band position shifted to higher wavenumber for RHC indicate the presence of defects in graphitic structure [33], which can be related with randomly packed carbon sub-units and disordered porous network.

The EDLCs constructed with the SGT_{12nm}, SGT_{8nm}, and RHC carbons in the binary mixture of ionic liquids [EMIm][FSI]_{0.5}[BF₄]_{0.5} electrolyte have been tested up to a voltage of 3.0 V and temperatures between 24 and $-40\text{ }^\circ\text{C}$ (see also Figure S1 and S2 in supporting information). Galvanostatic charge/discharge curves at $100\text{ mA}\cdot\text{g}^{-1}$ (per active carbon

in one electrode) are compared in Fig. 3 at various temperatures. The symmetric shape curves for all three cells show an essentially EDL charging behavior at room temperature. The RHC carbon-based cell owing to its high surface area displays longer charge/discharge time compared to cells with SGT_{12nm} and SGT_{8nm} carbons.

Considering the pore size range of RHC evaluated from the gas adsorption data in Fig. 1, a large fraction of micropores and small amount of mesopores constitute its surface area that serve as channels connecting the micropores for easy ionic transport. Therefore, the broad pore size distribution of RHC favors an efficient formation and charging of double-layer at room temperature. Certainly, the bigger pores facilitate the ion movement and these ions are stored at the EDL in the narrow spaces of carbon porosity, where the confinement effects are more pronounced. Thanks to these surface and porous characteristics, a high RHC capacitance of $110\text{ F}\cdot\text{g}^{-1}$ is achieved at room temperature. In contrast, the pore structure of SGT_{12nm} and SGT_{8nm} is different, where micropores are distributed in the range from 0.7 to 1.5 nm. In case of SGT_{8nm} carbon, relatively big fraction of micropores is well-connected with bigger channels as evident from the gas adsorption data. On the other hand, SGT_{12nm} possesses ultramicropores that are less accessible via channels and appears to be ink-bottle type pores, while a small fraction of micropores are in the range of 1.0 nm. Overall, the accessible micropores in SGT_{12nm} are mainly of 1.0-nm range while for the SGT_{12nm}, the micropores are present from 0.7 to 1.5 nm. The ultramicropores where the EDL is formed

Fig. 3 Galvanostatic charge/discharge curves (specific current = $100\text{ mA}\cdot\text{g}^{-1}$, per active carbon in one electrode) of three EDLCs at different temperatures: (a) $24\text{ }^\circ\text{C}$; (b) $0\text{ }^\circ\text{C}$; (c) $-20\text{ }^\circ\text{C}$; (d) $-40\text{ }^\circ\text{C}$



are connected with big micropores for an ideal ion transport. This difference in microporous structure leads to slightly higher capacitance of $96 \text{ F}\cdot\text{g}^{-1}$ for $\text{SGT}_{8\text{nm}}$, compared to $92 \text{ F}\cdot\text{g}^{-1}$ for $\text{SGT}_{12\text{nm}}$ at room temperature (Fig. 4a, values extracted from charge/discharge curves in Fig. 3).

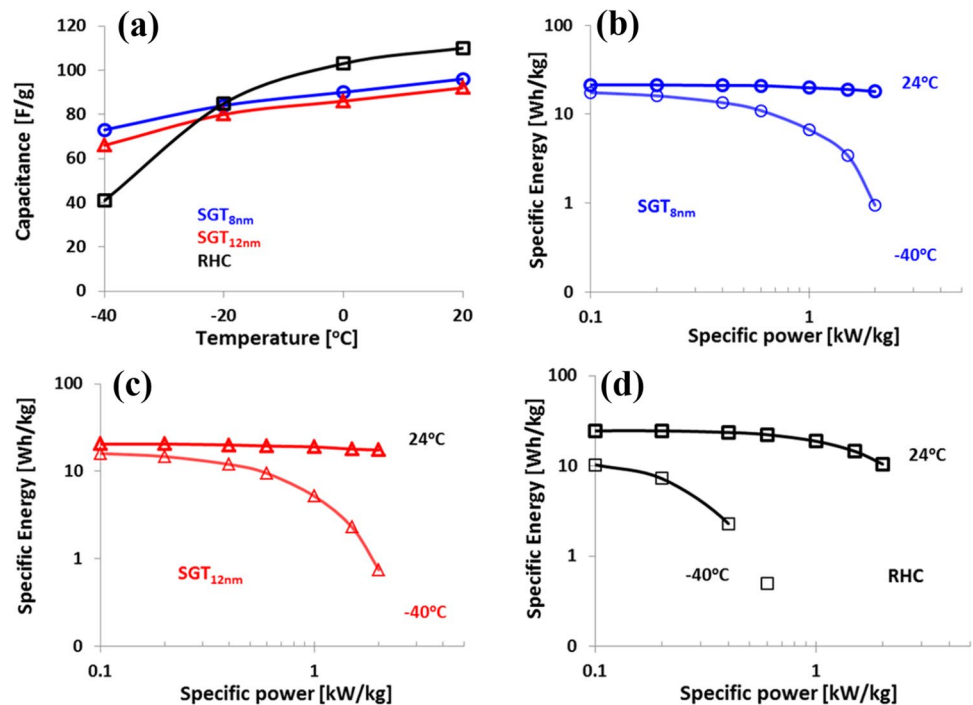
Clearly, the porosity data in the mesoporous region is comparable for two hierarchical carbons with main fraction of up to 85% constituting the mesopores which favors the ions transport towards small pores. However, the difference in the microporous region leads to different confinement effects and the better screening of charges in case of $\text{SGT}_{8\text{nm}}$. The capacitance difference between these two hierarchical carbons originates due to the factor related with better charge accommodation and accumulation of co-ions in the pores. Under the absence of electrochemical polarization, the coulombic disorder leading to the so-called superionic state is more favored in $\text{SGT}_{8\text{nm}}$ due to the presence of pores in the range of 0.7 nm which are easily accessible via big micropores. This effect is less pronounced in case of $\text{SGT}_{12\text{nm}}$ where pores around 0.7 nm are not easily accessible for the large EMIm^+ cations and FSI^- and BF_4^- anions. These ions are then accumulated at relatively larger pores around 1.0 nm where the confinement effects are probably absent (the breaking of ionic arrangement is less favored) and consequently co-ions are pushed out of the pores, thus hindering the co-ion pair formation. In the context of ionic ordering, (i) firstly, the arrangement of ions is broken due to the use of mixture of ILs where different anions drive the interaction of ions and pore wall in a completely different manner than in neat ILs. Secondly, the confinement

of binary mixture in the nanopores leads to even enhanced disorder, favorable for the formation of co-ion pair. Furthermore, under the electrochemical polarization, two different types of anions (FSI^- and BF_4^-) are desorbing/adsorbing which play an important role in the EDL structure and determine the performance of a supercapacitor [34].

When decreasing temperature, the performance of RHC-based cell deteriorates faster than the EDLCs with $\text{SGT}_{8\text{nm}}$ and $\text{SGT}_{12\text{nm}}$. The former displays only $41 \text{ F}\cdot\text{g}^{-1}$ down to -40°C and we correlate this capacitance decay of RHC with the presence of majority of pores in the range of 0.7–2.0 nm where the diffusion of IL-based electrolyte is strongly affected at low temperatures. In contrast, for $\text{SGT}_{8\text{nm}}$ and $\text{SGT}_{12\text{nm}}$, the presence of wide transport channels at around 6–8 nm maintains bulk electrolyte-like properties, favors the ionic penetration, and reduces the impact of diffusion limitations at low temperature. Consequently, higher capacitance values are achieved for EDLCs with $\text{SGT}_{8\text{nm}}$ and $\text{SGT}_{12\text{nm}}$ carbons compared to the one with RHC. Nevertheless, it can be seen that EDLC with $\text{SGT}_{8\text{nm}}$ electrodes exhibits a higher capacitance output ($73 \text{ F}\cdot\text{g}^{-1}$) than $\text{SGT}_{12\text{nm}}$ ($66 \text{ F}\cdot\text{g}^{-1}$) down to -40°C which is related with a relatively large mesopore volume and better hierarchical porous structure in the former.

Despite an increase of electrolyte viscosity which is evident from the ohmic loss seen from the charge/discharge curves for all the cells operating down to low temperatures, this effect is more pronounced in case of $\text{SGT}_{12\text{nm}}$ than in $\text{SGT}_{8\text{nm}}$. Note that the difference of capacitance between the EDLCs containing two hierarchical carbons increases with

Fig. 4 **a** Specific capacitance (expressed per active carbon in one electrode) versus temperature. **b–d** Ragone plots extracted from constant power tests (up to $2 \text{ kW}\cdot\text{kg}^{-1}$) at 24°C and -40°C for three EDLCs up to a voltage of 3.0 V



a decrease of temperature. Here, the main factor influencing the performance of EDLCs at low temperature is the diffusion limitations of ionic species through the narrow spaces. This is evident from a large capacitance decay of 60% in case of RHC going from 0 to $-40\text{ }^{\circ}\text{C}$ and the main reason being the absence of big mesopores. As a result, the electrolyte does not maintain a bulk-like state at low temperatures in the pores of RHC. This finding is further supported by relatively small capacitance decay of 19% and 23% (going from 0 to $-40\text{ }^{\circ}\text{C}$) for EDLCs with SGT_{8nm} and SGT_{12nm}, respectively. The presence of large volume of mesopores in both hierarchical carbons from 6 to 13 nm provides big channels for the IL-based mixture to keep bulk electrolyte-like properties which is only slightly influenced by the diffusion limitations. Clearly, the large mesopores in SGT_{8nm} and SGT_{12nm} are the reason of efficient EDL formation and excellent electrochemical performance down to $-40\text{ }^{\circ}\text{C}$.

Figure 4b–d show a comparison of specific energy versus specific power values for each EDLC at $24\text{ }^{\circ}\text{C}$ and $-40\text{ }^{\circ}\text{C}$. Thanks to the high surface area and developed pore structure of SGT_{8nm}, a high specific energy of $18\text{ Wh}\cdot\text{kg}^{-1}$ was received at $2\text{ kW}\cdot\text{kg}^{-1}$ (at $24\text{ }^{\circ}\text{C}$) which is slightly higher than the values for EDLC with SGT_{12nm}. However, a significant difference is noted in energy values at $-40\text{ }^{\circ}\text{C}$, where EDLC with SGT_{8nm} showed $3.5\text{ Wh}\cdot\text{kg}^{-1}$ compared to $2.3\text{ Wh}\cdot\text{kg}^{-1}$ for SGT_{12nm} at $1.5\text{ kW}\cdot\text{kg}^{-1}$. The cell with RHC, on the other hand, with highest energy value of $24.5\text{ Wh}\cdot\text{kg}^{-1}$ at $24\text{ }^{\circ}\text{C}$ and $0.1\text{ kW}\cdot\text{kg}^{-1}$ did not display any energy value beyond $0.6\text{ kW}\cdot\text{kg}^{-1}$ at $-40\text{ }^{\circ}\text{C}$ due to the reason discussed in previous sections. From the foregoing, it is clear that apart of keeping high mobility of charge carriers in the bulk electrolyte, an appropriate optimization of porous structure towards effective dimensions of guest molecules and ions is also critical for advanced performance of EDLCs operating at low temperatures. For this reason, it is important to design new porous carbon materials with appropriate ratio of meso- and micropores to suppress the diffusion limitations and improve the performance.

Conclusion

The pore structure of carbons plays a key role in determining their electrochemical performance. This work shows that at room temperature, the coulombic ordering in the narrow spaces of micropores (below 1.0 nm) determines the capacitance of EDLC using IL-based electrolyte. Thus, even small changes in microporosity of hierarchical carbons can bring significant difference in their capacitance. Whereas, mesopores in the range of 6–13 nm are crucial for the enhanced performance of EDLCs using ionic liquid-based electrolytes at low temperatures. A high fraction of mesopores facilitates the ionic movement and reduces

the diffusion limitations as well as allows the IL mixture to keep bulk-like properties. Nevertheless, pore wall interaction with large ions might lead to partial IL freezing which is more evident in strongly microporous carbons that lack large channels for efficient ionic transport.

SiO₂ template is a viable method to design relatively high surface area carbons with hierarchical pores. The surface properties of the carbons can be tuned by changing the template nanoparticle size. Hierarchical porosity and balanced ratio of micro- and mesopores can be achieved by exploring new template materials. This is essentially related with controlling the size of graphene sub-units produced from the leaching of uniform silica nanoparticles. Thus, in order to design high-energy EDLCs adapted for operating at low temperatures, it is recommended to optimize the architecture of carbon porosity along with electrolyte composition towards matching the pore geometries with the effective dimensions of the ions comprising the ionic liquids for facile EDL formation at ambient temperature and efficient transport at low temperatures.

Supplementary Information The online version contains supplementary material available at <https://doi.org/10.1007/s11581-021-04354-w>.

Acknowledgements The authors acknowledge the contributions of Dr. Harald Fitzek (FELMI-ZFE, Austria) and Askhat Beldeubayev from the core facilities of Nazarbayev University in experimental work and data analysis.

Funding Open access funding provided by Graz University of Technology. V.P. acknowledges the funding from the Ministry of Education and Science of the Republic of Kazakhstan (grant no. AP08956403). A. Ng acknowledges the grants from the Ministry of Education and Science of the Republic of Kazakhstan (grant no. AP08856931) and Nazarbayev University (grant no. 021220CRP0422). Q.A. and V.P. thank the Austrian Agency for International Cooperation in Education and Research (OeAD-GmbH) for awarding mobility funds in EPU-Projekt Call 2019. D.K. thanks the European Union's Horizon 2020 research program under Grant Agreement No. 823717-ESTEEM3.

Open Access This article is licensed under a Creative Commons Attribution 4.0 International License, which permits use, sharing, adaptation, distribution and reproduction in any medium or format, as long as you give appropriate credit to the original author(s) and the source, provide a link to the Creative Commons licence, and indicate if changes were made. The images or other third party material in this article are included in the article's Creative Commons licence, unless indicated otherwise in a credit line to the material. If material is not included in the article's Creative Commons licence and your intended use is not permitted by statutory regulation or exceeds the permitted use, you will need to obtain permission directly from the copyright holder. To view a copy of this licence, visit <http://creativecommons.org/licenses/by/4.0/>.

References

1. Lewandowski A, Olejniczak A, Galinski M, Stepniak I (2010) Performance of carbon-carbon supercapacitors based on

- organic, aqueous and ionic liquid electrolytes. *J Power Sources* 195:5814–5819
2. Presser V, Heon M, Gogotsi Y (2011) Carbide-derived carbos – from porous network to nanotubes and graphene. *Adv Funct Mater* 21:810–833
 3. Lin R, Taberna P-L, Fantini S, Presser V, Perez CR, Malbosc F, Rupesinghe NL, Teo KB, Gogotsi Y, Simon P (2011) Capacitive energy storage from -50 to 100°C using an ionic liquid electrolyte. *J Phys Chem Lett* 2:2396–2401
 4. Vatamanu J, Xing L, Li W, Bedrov D (2014) Influence of temperature on the capacitance of ionic liquid electrolytes on charged surfaces. *Phys Chem Chem Phys* 16:5174–5182
 5. Tsai W-Y, Lin R, Murali S, Li Zhang L, McDough J, Ruoff R, Taberna P-L, Gogotsi Y, Simon P (2013) Outstanding performance of activated graphene based supercapacitors in ionic liquid electrolyte from -50 to 80 °C. *Nano Energy* 2:403–411
 6. Kunze M, Jeong S, Paillard E, Winter M, Passerini S (2010) Melting behavior of pyrrolidinium-based ionic liquids and their binary mixtures. *J Phys Chem C* 114:12364–12369
 7. Kunze M, Jeong S, Appetecchi G, Schönhoff M, Winter M, Passerini S (2012) Mixtures of ionic liquids for low temperature electrolytes. *Electrochim Acta* 82:69–74
 8. Eliad L, Salitra G, Soffer A, Aurbach D (2001) Ion sieving effects in electrical double layer of porous carbon electrodes: estimating effective ion size in electrolytic solutions. *J Phys Chem B* 105:6880–6887
 9. Shilina Y, Levi M, Dargel V, Aurbach D, Zavorine S, Nucciarone D, Humeniuk M, Halalay I (2013) Ion size to pore width ratio as a factor that determines the electrochemical stability window of activated carbon electrodes. *J Electrochem Soc* 160:A629–A635
 10. Futamura R, Iiyama T, Takasaki Y, Gogotsi Y, Biggs M, Salanne M, Ségalini J, Simon P, Kaneko K (2017) Partial breaking of the Coulombic ordering of ionic liquids confined in carbon nanopores. *Nat Mater* 16:1225–1232
 11. Yan R, Antonietti M, Oschatz M (2018) Toward the experimental understanding of the energy storage mechanism and ion dynamics in ionic liquid based supercapacitors. *Adv Energy Mater* 8:1800026
 12. Hiraoka T, Othani R, Nakamura M, Lindoy L, Hayami S (2019) Water-induced breaking of the Coulombic ordering in a room-temperature ionic liquid metal complex. *Chem A Eur J* 25:7521–7525
 13. Kondrat S, Georgi N, Fedorov M, Kornyshev A (2011) A superionic state in nano-porous double-layer capacitors: insights from Monte Carlo simulations. *Phys Chem Chem Phys* 13:11359–11366
 14. Kondrat S, Kornyshev A (2011) Superionic state in double-layer capacitors with nanoporous electrodes. *J Phys Condens Matter* 23:022201
 15. Prehal C, Koczwarza C, Jäckel N, Schreiber A, Burian M, Amenitsch H, Hartmann M, Presser V, Paris O (2017) Quantification of ion confinement and desolvation in nanoporous carbon supercapacitors with modelling and in situ X-ray scattering. *Nat Energy* 2:16215
 16. Levy A, Pedro de Souza J, Bazant M (2020) Breakdown of electroneutrality in nanopores. *J Colloid Interface Sci* 579:162–176
 17. Matthews R, Viller-Garcia I, Weber C, Griffith J, Cameron F, Hallett J, Hunt P, Welton T (2016) A structural investigation of ionic liquid mixtures. *Phys Chem Chem Phys* 18:8608–8624
 18. Brooks N, Castiglione F, Doherty S, Dolan A, Hill A, Hunt P, Matthews R, Mauri M, Mele A, Simonutti R, Viller-Garcia I, Weber C, Welton T (2017) Linking the structures, free volumes, and properties of ionic liquid mixtures. *Chem Sci* 8:6359–6374
 19. Yambou EP, Górska B, Béguin F (2021) Electrical double-layer capacitors based on a ternary ionic liquid electrolyte operating at low temperature with realistic gravimetric and volumetric energy output. *Chem Sus Chem* 14:1196–1208
 20. Fuertes A, Lota G, Centeno T, Frackowiak E (2005) Templated mesoporous carbons for supercapacitor application. *Electrochim Acta* 50:2799–2805
 21. Härmas M, Palm R, Thomberg T, Härmas R, Koppel M, Paalo M, Tallo I, Romann T, Jänes A, Lust E (2020) Hydrothermal and peat-derived carbons as electrode materials for high-efficient electrical double-layer capacitors. *J Appl Electrochem* 50:15–32
 22. Zhao J, Gorbatovski G, Oll O, Thomberg T, Lust E (2019) Effect of alkali and halide ion doping on the energy storage characteristics of ionic liquid based supercapacitors. *Electrochim Acta* 319:82–87
 23. Leyva-Garcia S, Lozani-Castello S, Morallon E, Vogl T, Schutter C, Passerini S, Balducci A, Cazorla-Amoros D (2016) Electrochemical performance of a superporous activated carbon in ionic liquid-based electrolytes. *J Power Sources* 336:419–426
 24. Annat G, Forsyth M, MacFarlane D (2012) Ionic liquid mixtures—variations in physical properties and their origins in molecular structure. *J Phys Chem B* 116:8251–8258
 25. Palm R, Kurig H, Tonurist K, Jänes A, Lust E (2012) Is the mixture of 1-ethyl-3-methylimidazolium tetrafluoroborate and 1-butyl-3-methylimidazolium tetrafluoroborate applicable as electrolyte in electrical double layer capacitors? *Electrochem Commun* 22:203–206
 26. Thommes M, Kaneko K, Neimark AV, Olivier JP, Francisco Rodriguez-Reinoso JR, Kenneth SW, Sing (2015) *Pure Appl Chem* 87: 1051–1069.
 27. Rouquerol F, Rouquerol J, Sing K (1999) *Adsorption by Powders and Porous Solids-Principles Methodology and Applications*. Academic Press, London, UK
 28. Krivchenko VA, Pilevsky AA, Rakhimov AT, Seleznev BV, Suetin NV, Timofeyev MA, Bepalov AV, Golikova OL (2010) Nanocrystalline graphite: promising material for high current field emission cathodes. *J Appl Phys* 107:014315
 29. Kim K, Lee T, Kwon Y, Seo Y, Song J, Park J, Lee H, Park J, Ihee H, Cho S, Ryoo R (2016) Lanthanum-catalysed synthesis of microporous 3D graphene-like carbons in a zeolite template. *Nature* 535:131–135
 30. Leyva-Garcia S, Lozano-Castello D, Morallon E, Cazorla-Amoros D (2016) Silica-templated ordered mesoporous carbon thin films as electrodes for micro-capacitors. *J Mater Chem A* 4:4570–4579
 31. Nishihara H, Kyotani T (2018) Zeolite-templated carbons – three-dimensional microporous graphene frameworks. *Chem Commun* 54:5648–5673
 32. Gao W, Wan Y, Dou Y, Zhao D (2011) Synthesis of partially graphitic ordered mesoporous carbons with high surface areas. *Adv Energy Mater* 1:115–123
 33. Gibot P, Schnell F, Schaefer M, Spitzer D (2019) Nanostructuring of carbon materials by means of a calcium phosphate template. *J Porous Mater* 26:747–754
 34. Forse A, Griffin J, Merlet C, Bayley P, Wang H, Simon P, Grey C (2015) NMR Study of ion dynamics and charge storage in ionic liquid supercapacitors. *J Am Chem Soc* 137:7231–7242

Publisher's Note Springer Nature remains neutral with regard to jurisdictional claims in published maps and institutional affiliations.